RSC Advances

PAPER

View Article Online
View Journal | View Issue

Cite this: *RSC Adv.*, 2024, **14**, 5331

Electron-donating arene-substituted pentacenedione derivatives: a study of structural, electronic, and electrochemical properties†

Eyad A. Younes, *[a] Yamen J. Hammad,[a] Fatemeh Salami, [b] Anas J. Rasras, [c] Raed A. Al-Qawasmeh[de] and Yuming Zhao [b]

Received 31st July 2023
Accepted 3rd February 2024

DOI: 10.1039/d3ra05173k

rsc.li/rsc-advances

A new series of redox-active tetraryl-substituted pentacenedione derivatives, namely Ar4-PDs, was prepared through Suzuki–Miyaura coupling reactions between a bis(dibromomethane)pentacenedione and various arene boronic acids. Single-crystal X-ray diffraction analysis and density functional theory (DFT) calculations have confirmed that these Ar4-PDs possess highly twisted conformations due to the significant steric encumbrance between the Ar substituents and the anthraquinodimethane moiety. Cyclic voltammetric analysis revealed that the nature of the Ar group critically influences the redox properties of Ar4-PDs. In the case where the Ar group is a strong electron donor, triphenylamino (TPA), the Ar4-PD derivative exhibits an amphoteric redox behavior with a narrowed electrochemical band gap (1.38 eV) and a noticeable intramolecular charge transfer (ICT) band in the visible region of the spectrum. The twisted molecular conformation is believed to facilitate through-space interactions between the donor (TPA) and acceptor (anthraquinone) groups, while protonation of this compound with a strong organic acid can further enhance the ICT effect.

1 Introduction

The family of donor–acceptor (D–A) organic molecules has undergone a spectacular expansion in recent years, owing to their increasingly important applications in molecular electronics and optoelectronics.[1–4] A wide range of recently designed organic D–A compounds has been found to show properties useful for organic light-emitting diodes (OLEDs),[5–7] organic photovoltaics (OPVs),[8–10] organic field-effect transistors (OFETs),[11–13] photoinitiators in polymerization,[14,15] and so on. Typically, a D–A molecular system can be assembled by linking an electron-donating (D) group with an electron-accepting (A) group through either a π-conjugated or a non-conjugated bridging unit. Numerous π-conjugated D–A systems have been designed with a planar molecular conformation in order to achieve enhanced optoelectronic performance such as narrowed band gaps, large hyperpolarizabilities, and long-lived charge-separation states.[16–18] On the other hand, the application of planar-shaped π-systems in device fabrication faces some challenges, one of them being low solubility/processability as a result of their strong intermolecular π–π stacking.[19,20] This problem can be solved by incorporation of solubilizing side chains (*e.g.*, alkyl groups) to the framework of the molecule.[21] However, such molecular tailoring strategy has pros and cons for device performance. Studies have shown that side chains can significantly alter the molecular packing mode of a D–A system in the solid state to cause substantial changes in photophysical and electrochemical properties that are desirable for device application.[22,23] For example, Tu and co-workers recently examined D–A conjugated small molecules with different side chain lengths as potential perovskite solar cells (PSCs). Their results showed that shortening the side chain is conducive to improving the thin film quality of these compounds.[24]

Besides the side-chain strategy, twisting the backbone of a π-conjugated molecule into a non-planar conformation presents another effective method for coping with the solubility/processability challenge that many planar π-conjugated D–A systems face.[25–27] For example, a twisted furan-based organic material was reported by Nakahara *et al.* as a solution-processable organic semiconductor.[28] The twisted

[a]*Department of Chemistry, Faculty of Science, The Hashemite University, P. O. Box 330127, Zarqa 13133, Jordan. E-mail: e.younes@hu.edu.jo; Tel: +962 5 3903333 ext. 4572*

[b]*Department of Chemistry, Memorial University of Newfoundland, St. John's, NL, A1C 5S7, Canada*

[c]*Department of Chemistry, Faculty of Science, Al-Balqa Applied University, P. O. Box 19117, Al-Salt, Jordan*

[d]*Pure and Applied Chemistry Research Group, College of Science, Department of Chemistry, University of Sharjah, P. O. Box 27272, Sharjah, United Arab Emirates*

[e]*Department of Chemistry, The University of Jordan, Amman 11942, Jordan*

† Electronic supplementary information (ESI) available: ^{1}H and ^{13}C NMR spectra for new compounds **5a–d**, single-crystal XRD data for **3a** and **5c**, control UV-vis experimental results, and DFT calculations performed on **5a**. CCDC 2284400 and 2284398. For ESI and crystallographic data in CIF or other electronic format see DOI: https://doi.org/10.1039/d3ra05173k

conformation of this compound renders it highly soluble in most organic solvents, while the single-crystal field-effect transistor built upon it achieved a hole mobility of up to 1.0 $cm^2 V^{-1} s^{-1}$. Actually, the conformational twisting method is particularly useful for manipulating functional molecules that contain polycyclic aromatic hydrocarbon (PAH) cores. Through this strategy, a variety of twisted D–A molecules have been prepared and investigated as novel organic semiconducting materials. Studies have demonstrated that twisting of the shapes of π-conjugated organic molecules could avoid the formation of the most common herringbone π-stacking motif in the solid state, hence facilitating efficient charge-carrier transport in organic semiconductors.[29,30]

Among numerous D/A molecular building blocks, quinone represents a popular acceptor motif due to its excellent redox activity.[31–33] Quinone shows a proaromatic character in the neutral state. Upon two-electron reduction, quinone can be converted into an aromatic dianion, rendering it with relatively low reduction potentials and good electrochemical reversibility.[34] When quinone is embedded in linear acene structures, various quinoidal π-acceptors are formed, such as anthraquinone (AQ),[35] tetracenedione (TD),[36] and pentacenetetraones (PT).[37] Among these derivatives, pentacene-5,7,12,14-tetraone (**1**, Scheme 1) is an intriguing compound that can serve as a versatile springboard toward novel redox-active D/A molecular systems. **PT 1** itself has a fully planar molecular conformation, making it readily undergo π–π stacking and thus show limited solubility in the solution phase.[38] It has been demonstrated that one of the quinone units in **1** can selectively undergo a two-fold Ramirez dibromoolefination reaction to yield 7,12-bis(dibromomethylene)-7,12-dihydropentacene-5,14-dione (**2**). In this reaction, the quinone group is converted into a quinodimethane moiety with increased steric hindrance around it. As a result, the central pentacene structure of **2** favors to take a non-planar, kinked shape. Recently, Ishigaki *et al.*[39] performed Suzuki–Miyaura cross-coupling reactions on **2** to generate two phenyl-functionalized pentacenedione derivatives, compounds **3a–b** (see Scheme 1). These compounds were then used as precursors to prepare a series of octaaryl-substituted bisquinodimethanes with a zig-zag molecular conformation and three-stage redox activity. In 2021, Abdollahi and Zhao[40] performed double *S*-vinylation reactions on **2** to incorporate two electron-donating 1,4-dithiafulvenyl groups into the PD structure. The resulting D–A systems **4a–c** (Scheme 1) are highly redox active and show a twisted conformation with doubly curved π-surfaces. Co-crystallization of **4c** with C_{70} fullerene afforded ordered supramolecular assemblies through concave–convex complementarity.

As for organic π-donors, numerous research efforts have been focused on the design and synthesis of triphenylamine (TPA) derivatives, since the physicochemical properties of this class of compounds can be flexibly tuned through attachment of electron-donating or electron-accepting groups.[41–44] TPA derivatives have found applications as dye sensitizers in solar cells,[45] organic semiconductors,[46,47] electroluminophores in organic light-emitting diodes,[48] and superior photosensitizer.[49] Very recently, Sau and Samanta reported the synthesis of TPA–anthraquinone-based D–A hypercrosslinked polymers *via* Suzuki–Miyaura cross-coupling reaction between tris(4-(4,4,5,5-tetramethyl-1,3,2-dioxaborolan-2-yl)phenyl)amine and 2,6-dibromoanthracene-9,10-dione. Interestingly, the polymer showed photocatalytic activity to transform phenylboronic acid into phenol in yields up to 96%.[50]

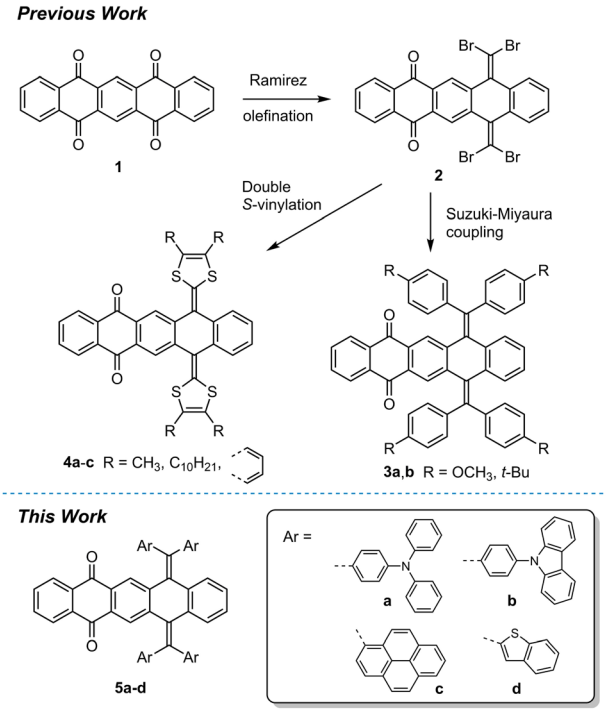

Scheme 1 Derivatization of twisted D–A systems based on pentacene-5,7,12,14-tetraone.

At the outset of this study, we envisioned that PD derivative **2** would offer synthetic access to more highly twisted D–A structures through transition-metal catalyzed coupling reactions taking advantage of its four reactive C(sp^2)–Br bonds. This type of derivation has never been reported prior to this work. So, to further explore this potential, we have designed and synthesized four new tetraarene-substituted PD derivatives **5a–d** as outlined in Scheme 1. Hereafter, these compounds are referred to as Ar4-PDs. The Ar groups chosen in our study range from triphenylamine (TPA), 9-phenylcarbazole (PhCBz), 1-pyrenyl (PY), and benzo[*b*]thiophene (BT) groups, respectively. These electron-donating groups possess significant steric crowdedness. As such, they were expected to induce highly twisted molecular structures when functionalized onto the PD unit, giving rise to π-conjugated topology that is dramatically different from that of a planar D–A molecular system. Investigations on these Ar4-PD compounds would further deepen our understanding of the intramolecular charge transfer (ICT) effect and foster new design ideas for advanced redox-active organic π-conjugated materials.

2 Results and discussion

2.1 Synthesis and structural elucidation

The synthetic approach to the target compounds, **5a–d**, is illustrated in Scheme 2. At the beginning, tetrabromo-substituted **PD 2** was subjected to Suzuki-Miyaura coupling

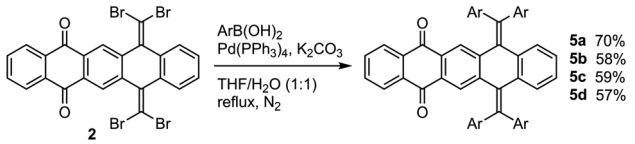

Scheme 2 Synthesis of Ar4-PD derivatives **5a–d** *via* Suzuki–Miyaura coupling reactions.

with corresponding areneboronic acids under the catalysis of $Pd(PPh_3)_4$ with K_2CO_3 as the base.[37,51] The coupling reactions were carried out at reflux using a mixture of THF and water (1 : 1, v/v) as the solvent. All the reactions went smoothly and were accomplished within *ca.* 7 hours, affording the target compounds in satisfactory yields (58% to 70%). Compounds **5a–d** showed good solubility in common organic solvents and they could be readily purified by silica flash column chromatography.

The molecular structures of **5a–d** were validated by NMR, MS, and FTIR analyses (see the ESI† for detailed spectroscopic characterization data). For comparison purposes, compound **3a** was also synthesized and characterized. To better understand the molecular conformational properties of the Ar4-PD system, attempts were made to grow their single crystals by a method of slow solvent evaporation. Among the five compounds, single crystals of **3a** and **5c** were successfully obtained and their structures were subsequently determined by X-ray diffraction (XRD) analysis.

Fig. 1 shows the molecular structures of **3a** and **5c** elucidated based on X-ray analysis. For each of the compounds, the central pentacene moiety takes a kinked shape as a result of the steric encumbrance between the quinodimethane unit and the four arene substituents. The anthraquinone segment, on the other hand, is not susceptible to any significant steric effects and thus retains a planar shape. For compound **5c**, the bulky pyrenyl groups also show notable steric clashing across the central quinodimethane unit. As a result, the quinodimethane moiety of **5c** shows a slightly lesser degree of distortion in comparison with compound **3a**.

^{1}H NMR analysis allows the conformational properties of Ar4-PDs to be examined in the solution phase. As can be seen in Fig. 2, the central phenyl ring of the Ar4-PD structure has two equivalent protons, which are labeled as Ha and Ha′, respectively. They give rise to a singlet signal in the aromatic region. Structurally, these two protons are in proximity to the adjacent Ar groups and therefore susceptible to the diamagnetic anisotropic effects delivered by the Ar groups. It is noteworthy that the least hindered compound **3a** shows a singlet peak (labeled with an asterisk mark in Fig. 2) at 7.86 ppm, while the other aromatic signals exhibit relatively sharp and well-resolved spectral patterns. The ^{1}H NMR spectrum of **3a** indicates that its molecular structure is somewhat flexible, allowing its conformers to rapidly equilibrate at the NMR time scale.

The ^{1}H NMR spectrum of TPA-substituted derivative **5a** shows relatively broad lineshape. The aromatic signals due to the anthraquinone moiety show noticeable shifts relative to **3a**; in particular, the singlet due to Ha/Ha′ (δ 7.83) appears to be slightly upfield-shifted in comparison with that of **3a**. The results suggest that TPA groups exert more significant steric encumbrance around the PD framework, but the effects are not strong enough to enable the observation of discrete conformers by NMR at room temperature.

PhCBz and BT-substituted derivatives **5b–c** both show sharp and well-resolved signals in their ^{1}H NMR spectra. The characteristic central protons (Ha/Ha′) give singlets at 8.03 ppm (**5b**) and 8.24 ppm (**5d**), respectively. Relative to that of **3a**, the central protons of **5b** and **5c** are shifted towards downfield. A possible reason for such shifts is that Ha/Ha′ are close to the edges of the planar arene groups (CBz or BT), making Ha/Ha′ experience a deshielding effect.

PY-substituted derivative **5c** shows a very complex spectral pattern in the aromatic region of the ^{1}H NMR spectrum. As

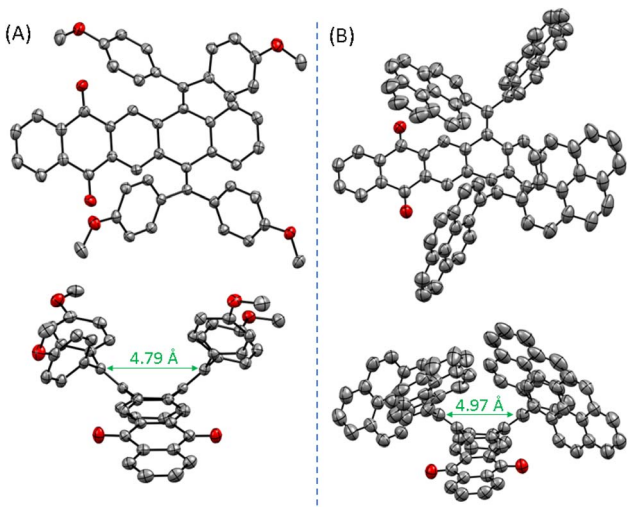

Fig. 1 ORTEP drawings (50% ellipsoid probability) of the molecular structures of (A) **3a** and (B) **5c** viewed from different perspectives. CCDC 2284400 and 2284398.

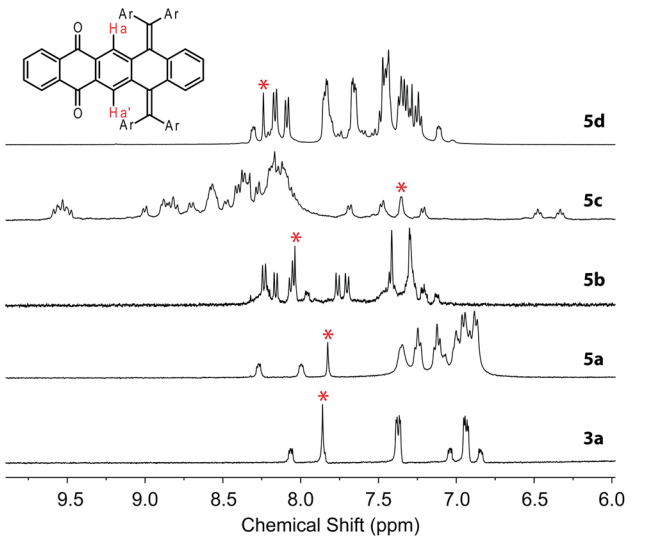

Fig. 2 Expanded ^{1}H NMR spectra of compounds **3a** and **5a–d** measured in DMSO-d_6 at room temperature.

shown in Fig. 2, most of the peaks of **5c** are broad in shape. Some peaks appear to be dramatically shifted towards either downfield or upfield in comparison with the spectra of other Ar4-PD derivatives. Of particular note is the singlet signal due to Ha/Ha′, which shows up at 7.36 ppm. In the X-ray structure of **5c**, the two protons Ha/Ha′ are observed to be close to the central regions of adjacent pyrene units. Such a structure suggests that pyrene units would exert strong deshielding effects on these two protons, making them the most upfield-shifted among the Ar4-PD derivatives examined in this work.

2.2 Electrochemical redox properties

The electrochemical redox properties of compounds **3a** and **5a–d** were investigated by cyclic voltammetry (CV). Fig. 3 shows the cyclic voltammograms of these compounds measured by scanning in the positive and negative potential windows, respectively. The CV data clearly show that the redox behaviors of Ar4-PDs are dependent on the nature of the Ar group. Scanning **3a** in the positive potential window, a weak anodic peak emerges at +1.25 V and a cathodic peak at +0.52 V. They are due to the electron transfer taking place on the electron-donating anisole groups in **3a**. In the negative potential window, the voltammogram of **3a** shows two cathodic peaks −0.78 V and −1.22 V, respectively. These two peaks can be assigned as stepwise reduction of the anthraquinone moiety.[52] In the reverse scan, there are no significant anodic peaks observed, indicating that the reduction process is electrochemically irreversible.

The voltammograms of **5a** shows a quasi-reversible redox wave pair at +1.18 V and +0.90 V in the positive potential window. This redox feature is due to the oxidation of electron-donating TPA groups in **5a**.[53] In the negative potential window, the voltammogram of **5a** shows a significant cathodic peak at −0.94 V, which can be ascribed to a simultaneous two-electron transfer on the anthraquinone moiety. The reduction process is irreversible, since there are no significant anodic peaks observed in the reverse scan.

For PhCBz-substituted **5b**, there are no obvious redox features in the positive potential window. In the negative potential window, a redox wave pair appears at $E_{pc} = -0.93$ V and $E_{pa} = -0.52$ V, which are due to simultaneous two-electron transfers on the anthraquinone moiety. Unlike the case of **5a**, the electrochemical reduction on **5b** is a quasi-reversible process.

PY-substituted compound **5c** shows an irreversible oxidation process with an anodic peak at +1.71 V in the positive potential window. This process is attributable to the oxidation of pyrene. In the negative potential window, the voltammogram of **5c** features two separate cathodic peaks at $E_{pc}{}^{1} = -0.79$ V and $E_{pc}{}^{2} = -1.16$ V, which are due to stepwise single-electron transfers occurring at the anthraquinone moiety. In the reverse scan, there is only one anodic peak at $E_{pa} = -1.03$ V, which is associated with the second cathodic peak at −1.16 V in the forward scan.

The CV profiles of BT-substituted **5d** disclose redox activity only in the negative potential window. It is interesting to note that there are two quasi-reversible redox wave pairs at $E_{pa}{}^{1} = -0.98$ V/$E_{pc}{}^{1} = -0.57$ V and $E_{pa}{}^{2} = -1.40$ V/$E_{pc}{}^{2} = -0.97$ V, respectively. They are attributable to stepwise single-electron transfers occurring on the anthraquinone moiety of **5d**.

It is worth remarking that three of the five Ar4-PDs here examined (**3a**, **5a**, and **5c**) exhibit clear amphoteric redox behaviors. According to the onset potentials in their first oxidation and reduction processes, the electrochemical band gaps (E_g) of these D–A molecular systems can be calculated as follows: 1.38 eV (**5a**), 1.48 eV (**3a**), and 2.39 eV (**5c**). Among them, TPA-substituted **5a** exhibits the narrowest band gap, which is in line with the observation of a long-wavelength ICT band in its UV-vis absorption spectrum (*vide infra*).

2.3 Electronic absorption properties

The electronic absorption properties of Ar4-PD derivatives, **3a** and **5a–d**, were examined by UV-vis spectroscopy. As shown in Fig. 4, the solution-phase absorption spectra of these compounds show significant absorption bands in the spectral region of 250 to 400 nm, which are characteristic of π → π* transitions. Among the five compounds, TPA-substituted **5a** shows the most redshifted absorption envelop, which concurs

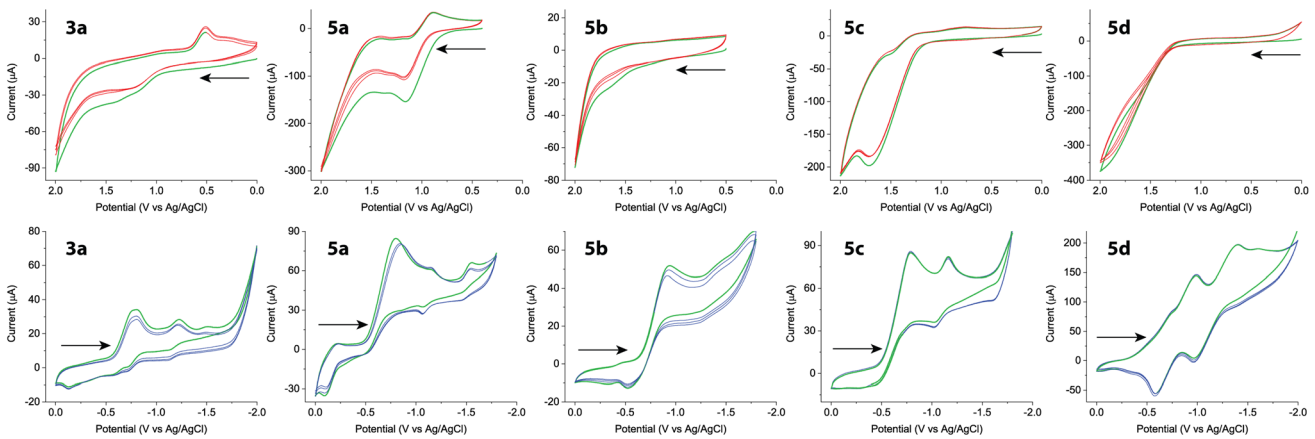

Fig. 3 Cyclic voltammograms of compounds **3a**, **5a–d** scanned in positive (top) and negative (bottom) potential windows, respectively. Experimental conditions: CH_2Cl_2 as solvent, Bu_4NBF_4 (0.1 M) as electrolyte, glassy carbon as the working electrode, Ag/AgCl as the reference electrode, and Pt wire as the counter electrode. Scan rate = 0.20 V s^{-1}.

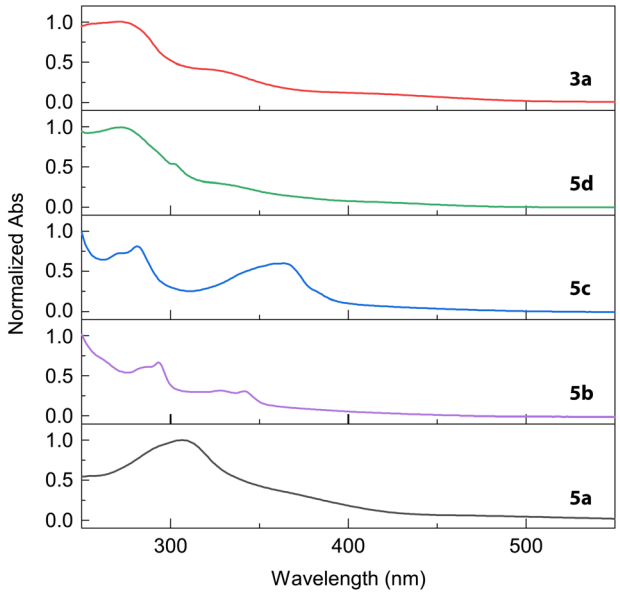

Fig. 4 UV-vis spectra of compounds **3a**, **5a–d** measured in $CHCl_3$ at room temperature.

with its narrow band gap determined by CV analysis. Close examination of the UV-vis spectrum of **5a** in the visible region reveals a weak, low-energy band centering around 710 nm (Fig. 5A). The absorbance of this band was found to comply with the Lambert–Beer's law (see the inset of Fig. 5A), ruling out the possibility that intermolecular aggregation is a cause for this long-wavelength absorption. The cutoff of this weak broad band is around 800 nm, corresponding to an optical band gap of 1.55 eV. The UV-vis determined band gap agrees well with that deduced from CV analysis, confirming that **5a** is a D–A system with a low HOMO–LUMO gap and hence may serve as a useful organic semiconductor.

Density functional theory (DFT) calculations showed that the HOMO and LUMO of **5a** are distributed in separate regions of the molecule. As can be seen from Fig. 5B, the HOMO of **5a** is mainly located around the two TPA groups that are adjacent to the anthraquinone unit, while the LUMO is predominantly distributed at the anthraquinone unit. The calculated HOMO–LUMO gap in the gas phase is 2.27 eV, which is higher than the experimentally determined ones by CV and UV-vis analyses. It is reasonable to attribute the lowest energy absorption band in the UV-vis spectrum of **5a** to an ICT origin, which involves an electronic transition from the HOMO to the LUMO.

Since the molecular structure of **5a** takes a highly twisted conformation as indicated by DFT calculations, the orbital interactions between TPA (donor) and anthraquinone (acceptor) should follow a through-space mechanism rather than through direct π-conjugation. We proposed that the steric hindrance around the anthraquinodimethane segment of **5a** forces two of the four TPA groups to move close to the anthraquinone moiety, resulting in intimate D–A interactions and thus an enhanced ICT effect. To validate this hypothesis, a control experiment was conducted in which pentacenedione derivative **2** was physically mixed with a TPA derivative in $CHCl_3$. The UV-vis spectrum of this D/A mixture did not show any CT bands like that observed in the spectrum **5a** (see the ESI† for details). The contrasting results confirmed that the ICT band of **5a** arises from intramolecular D–A interactions.

The ICT effect of **5a** can be further enhanced by protonation. It was observed that addition of a strong organic acid, trifluoroacetic acid (TFA), to a solution of **5a** resulted in a gradual increase in the ICT absorption band at 700 nm. As shown in Fig. 6, the increasing absorbance shows a nonlinear correlation with time and the trend of change fits well with a mono-exponential equation, suggesting a pseudo-first-order kinetic behavior. In the structure of **5a**, the amino and keto groups are both sensitive to protonation. In theory, protonation on the amino groups should result in diminished electron-donating effects and therefore cannot lead to enhancement in the ICT absorption band. On the contrary, protonation of the keto groups may further strengthen the electron-withdrawing power of the anthraquinone unit to enhance the ICT effect.

To better understand the reactivity of **5a** towards protonation, a comparative ^{1}H NMR study was carried out. In the

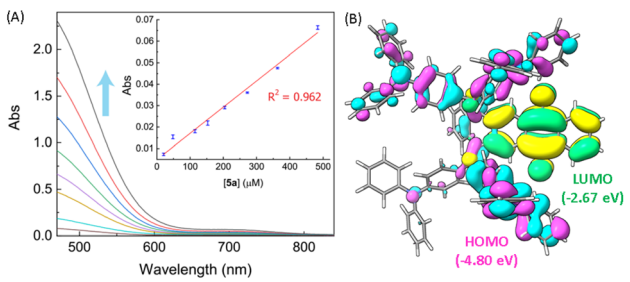

Fig. 5 (A) UV-vis spectra of compound **5a** measured in $CHCl_3$ at different concentrations. The arrow indicates the trend of increasing concentration. Inset: correlation of the absorbance at 710 nm with the concentration of **5a**. Data are fitted with linear regression. (B) Plots of HOMO and LUMO (isovalue = 0.02 au) **5a** calculated at the B3LYP/6-31G(d,p) level. HOMO: cyan/pink colored; LUMO: green/yellow colored.

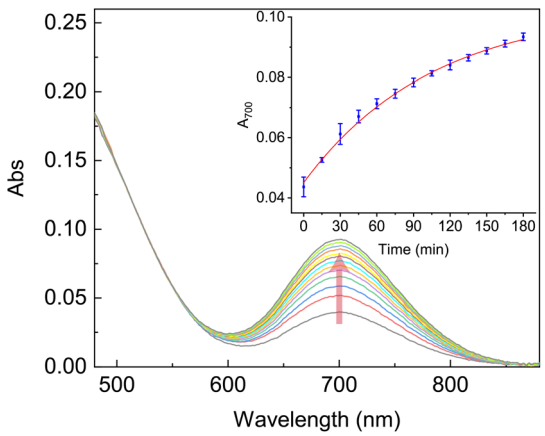

Fig. 6 UV-vis spectra of **5a** (55.0 μM in $CHCl_3$) mixed with TFA (4.0 mole equivalents) recorded at different time intervals. The arrow indicates the trend of change. Inset: plot of the absorbance at 700 nm (A_{700}) as a function of time (t, min). The red-color trace shows the curve fitting with a mono-exponential nonlinear equation, $y = y_0 + C \times e^{-kx}$, where $k = 105.32 \pm 7.04$ min^{-1} and $R^2 = 0.998$.

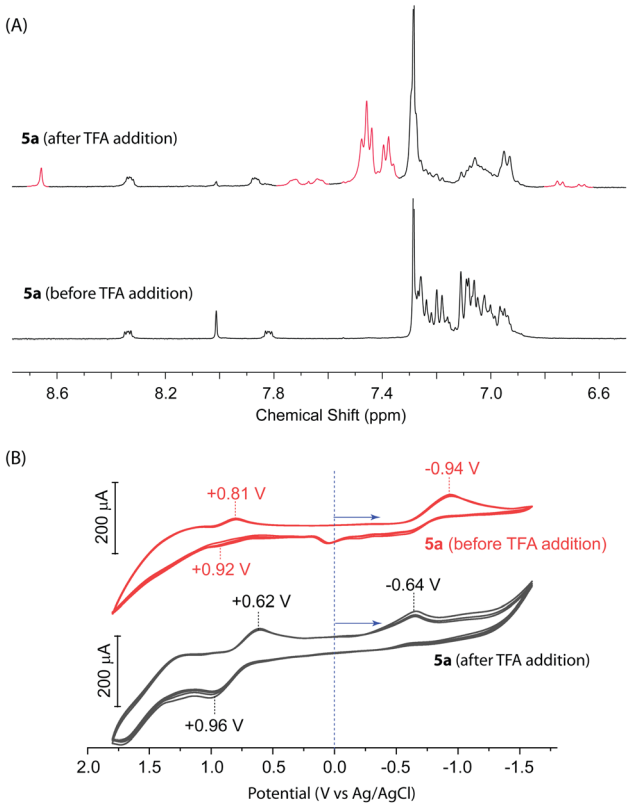

Fig. 7 (A) ^{1}H NMR (400 MHz, $CDCl_3$) spectra of **5a** measured before (bottom trace) and after (top trace) mixing with excess TFA for 24 hours. New peaks emerging after protonation are highlighted by red color. (B) Multi-cycle CV scans of **5a** before and after mixing with excess TFA in CH_2Cl_2. The arrows indicate the direction of the initial scan (starting from 0.0 V). Bu_4NBF_4 (0.1 M) as electrolyte, glassy carbon as the working electrode, Ag/AgCl as the reference electrode, and Pt wire as the counter electrode. Scan rate = 0.20 V s^{-1}.

experiment, **5a** was first protonated with excess TFA for 24 hours and then recorded by ^{1}H NMR. The spectrum was compared with that of **5a** before protonation. From the two spectra shown in Fig. 7A, one can clearly see that new aromatic signals emerge significantly after protonation of **5a**. Among the signals, a sharp singlet can be distinctively observed at 8.66 ppm, which is due to the two equivalent protons (Ha/Ha′) on the central ring of the pentacene unit. Protonation of **5a** causes a downfield shift of Ha/Ha′, suggesting that they are in a more deshielding environment than its neutral form. Additionally, certain protons on the TPA groups can be seen to show notable downfield shifts after protonation.

The effects of protonation on **5a** were also examined by CV analysis. As shown in Fig. 7B, the reduction potential of **5a** in the negative potential window is decreased by 0.30 V after protonation with TFA. This significant change suggests that the anthraquinone group was protonated to gain enhanced electron-withdrawing ability. In the positive window, the anodic peak due to the oxidation of TPA does not show very significant changes, indicating that the amino group of TPA is not an active site for protonation. Based on the experimental results, a protonation-enhanced ICT mechanism can be proposed (see Scheme 3).

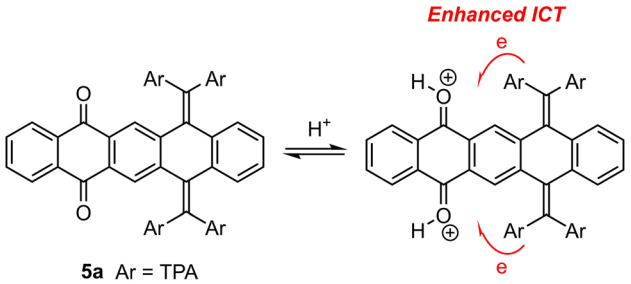

Scheme 3 Proposed mechanism for protonation-enhanced ICT on **5a**.

In this mechanism, protons first diffuse into the anthraquinone group to form protonated anthraquinone. This step is assumed to be relatively slow in view of the steric bulkiness of **5a** as well as the time-dependent growth of the ICT band in Fig. 6. Once the keto groups are protonated, their enhanced electron-withdrawing ability promotes more efficient ICT between TPA and anthraquinone, resulting in an enhanced long-wavelength absorption band around 700 nm in the UV-vis spectrum.

3 Conclusions

In summary, we herein present a systematic study of a series of new redox-active Ar4-PD derivatives. Our experimental results have clearly demonstrated that these compounds can be readily prepared through Suzuki–Miyaura coupling reactions. The Ar groups attached to the anthraquinodimethane unit create significant steric effects, leading to highly twisted molecular conformations as evidenced by crystallographic analysis and DFT calculations. The electrochemical redox behavior of the Ar4-PD is dependent on the nature of the Ar group, which offers a molecular approach to fine-tune the electronic properties of this type of D–A system. The most interesting finding of this work comes from the TPA-substituted Ar4-PD. In the molecule of **5a**, bulky TPA groups act as efficient electron donors to interact with the electron-withdrawing anthraquinone moiety *via* a through-space mechanism. An ICT effect arises from the intramolecular D–A interactions, leading to a narrow electrochemical band gap and a long-wavelength absorption band in the visible region of the spectrum. Moreover, the ICT effect in **5a** can be further enhanced through protonation. This property is beneficial for the development of stable vis-NIR chromophores with tolerance to acidity. We therefore anticipate that TPA-substituted **5a** can be applied as an efficient organic dye for advanced optoelectronic applications, such as light-harvesting, photocatalysis, and dye-sensitization of semiconducting nanoparticles.

4 Experimental details

4.1 Materials and instrumentation

All chemicals, solvents and reagents were obtained of standard quality from commercial suppliers (Sigma-Aldrich, Fluka, Acros, and Tedia) and were used as received without any further purification. All reactions were conducted in standard, dry glassware and under an inert atmosphere of nitrogen unless otherwise noted.

Melting points (mp) were determined using a Stuart Scientific (Britain) melting point apparatus with samples placed in one-end open glass capillaries. Thin-layer chromatography (TLC) was performed with silica gel F254 covered on aluminum sheets and visualized by UV light. ^{1}H and ^{13}C NMR spectra were recorded at room temperature on a Bruker III 400 MHz ADVANCE spectrometer. Chemical shifts (δ) are reported in ppm downfield relative to the signal of an internal reference ($SiMe_4$). Coupling constants (J) are given in Hz. Fourier transform infrared (FTIR) spectra were recorded on a Bruker Vertex 70 instrument. UV-vis absorption spectra were recorded on a Cary 100 Bio spectrophotometer. High-resolution APPI-TOF MS analysis was conducted on a Micromass GCT Premier instrument. Cyclic voltammetric (CV) analyses were carried out in a standard three-electrode setup controlled by a BASi Epsilon potentiostat. Single-crystal XRD data was collected at 100(2) K on a XtaLAB Synergy-S, Dualflex, HyPix-6000HE diffractometer using Cu Kα radiation (λ = 1.5406 Å). The crystal was mounted on nylon CryoLoops with Paraton-N. Data collection and reduction were processed within CrysAlisPro (Rigaku OD, 2020). A multi-scan absorption correction was applied to the collected reflections. Using the Olex2 (ref. 54) software package, structures were solved with the ShelXT[55] and ShelXL[56] programs.

Computational modeling studies were performed using the Gaussian 16 (rev. B01) software package.[57] Geometry optimization was done at the B3LYP/6-31G(d,p) level of theory and frequency calculations were performed at the same level of theory. The optimized structures were validated as energy minima by the absence of imaginary frequencies in their frequency calculations. Optimized molecular structures and frontier molecular orbitals were visualized using the UCSF ChimeraX program.[58]

4.2 Synthesis

7,12-Bis(dibromomethylene)-7,12-dihydropentacene-5,14-dione 2. Compound **2** was synthesized following the reported procedure.[51] Pentacene-5,7,12,14-tetraone (**1**, 0.30 g, 0.89 mmol), PPh_3 (2.3 g, 8.9 mmol), and CBr_4 (1.5 g, 4.5 mmol) were mixed in dry $CHCl_3$ (70 mL) under an atmosphere of N_2. The resulting mixture was refluxed overnight. The reaction mixture was subjected to filtration to remove insoluble byproducts. The filtrate was collected, washed with brine, and dried over $MgSO_4$. The organic layer was concentrated under vacuum to afford crude **2**, which was further purified by silica flash column chromatography (ethyl acetate/hexanes, 1 : 1) to give pure compound **2** as a pale yellow solid (0.36 g, 62%). Mp > 290 °C (decomp.). ^{1}H NMR (400 MHz, $CDCl_3$): δ 8.82 (s, 2H), 8.34 (dd, J = 5.7, 3.3 Hz, 2H), 7.91 (dd, J = 5.8, 3.3 Hz, 2H), 7.86–7.83 (m, 2H), 7.38 (dd, J = 5.8, 3.3 Hz, 2H).

General procedure for the synthesis of Ar4-PDs *via* Suzuki–Miyaura cross coupling. Compound **2** (0.40 g, 0.61 mmol) was mixed with $ArB(OH)_2$ (3.69 mmol) and K_2CO_3 (0.51 g, 3.69 mmol) in THF/H_2O (30 mL, 1 : 1). The reaction mixture was bubbled with nitrogen gas for 10 min. To the deoxygenated reaction mixture was then added $Pd(PPh_3)_4$ (0.024 g, 0.022 mmol). The reaction mixture was refluxed under nitrogen for 7 h and then cooled to rt. Next, the reaction mixture was extracted with chloroform. The organic layer was washed with brine, dried over $MgSO_4$, and then concentrated under vacuum. The resulting residue was subjected to silica flash column chromatography ($CHCl_3$/hexane, 1 : 1) to give pure Ar4-PD.

7,12-Bis(bis(4-methoxyphenyl)methylene)-7,12-dihydropentacene-5,14-dione (3a). Compound **3a** was obtained according to the reported procedure as a yellow solid. Mp > 300 °C (decomp.).[39] ^{1}H NMR (400 MHz, DMSO-d_6): δ 8.06 (dd, J = 5.8, 3.4 Hz, 2H), 7.86 (d, 3H), 7.37 (dd, J = 8.7, 2.9 Hz, 8H), 7.04 (dd, J = 5.9, 3.3 Hz, 2H), 6.94 (dd, J = 8.5, 3.6 Hz, 8H), 6.84 (dd, J = 5.7, 3.3 Hz, 2H), 3.75 (s, 6H), 3.71 (s, 6H). ^{13}C NMR (100 MHz, DMSO-d_6): δ 181.0, 157.5, 143.1, 141.5, 136.0, 133.5, 132.4, 132.2, 129.6, 128.9, 127.0, 125.9, 125.6, 125.0, 113.4, 113.1, 54.4, 54.4. FTIR (KBr): 2951, 1677, 1602, 1506, 1475, 1444, 1243, 1033 cm^{-1}. HRMS (APPI-TOF, positive mode) m/z calcd for $C_{52}H_{38}O_6$ 758.2668; found 758.2683 $[M]^{+\bullet}$.

7,12-Bis(bis(4-(diphenylamino)phenyl)methylene)-7,12-dihydropentacene-5,14-dione (5a). Compound **5a** was obtained according to the general procedure (0.56 g, 0.43 mmol) in 70% yield as a red solid. Mp = 185–188 °C. ^{1}H NMR (400 MHz, DMSO-d_6): δ 8.27 (dd, J = 5.8, 3.3 Hz, 2H), 8.00 (dd, J = 5.8, 3.3 Hz, 2H), 7.82 (s, 2H), 7.38–7.31 (m, 7H), 7.24 (t, J = 7.6 Hz, 9H), 7.10 (dt, J = 14.0, 6.7 Hz, 10H), 7.00 (q, J = 5.8, 5.0 Hz, 6H), 6.97–6.84 (m, 28H). ^{13}C NMR (100 MHz, DMSO-d_6): δ 182.2, 147.6, 147.4, 146.9, 146.6, 143.6, 142.9, 136.7, 136.1, 134.1, 133.5, 130.7, 130.6, 129.9, 129.8, 129.7, 129.6, 127.1, 125.1, 124.5, 124.3, 124.2, 123.8, 123.7, 123.5, 123.1, 122.3. FTIR (KBr): 3059, 1672, 1578, 1488 cm^{-1}. HRMS (APPI-TOF, positive mode) m/z calcd for $C_{96}H_{67}N_4O_2$ 1306.5186; found 1308.5377 $[M + H]^{+\bullet}$.

7,12-Bis(bis(4-(9*H*-carbazol-9-yl)phenyl)methylene)-7,12-dihydropentacene-5,14-dione (5b). Compound **5b** was obtained according to the general procedure (0.45 g, 0.35 mmol) in 58% yield as an orange solid. Mp = 235–237 °C. ^{1}H NMR (400 MHz, $CDCl_3$): δ 8.35–8.26 (m, 2H), 8.24 (s, 2H), 8.16 (d, J = 7.7 Hz, 4H), 8.09 (d, J = 7.7 Hz, 3H), 7.84 (dt, J = 9.8, 4.9 Hz, 8H), 7.66 (dd, J = 7.9, 3.0 Hz, 7H), 7.45 (dd, J = 10.1, 5.0 Hz, 13H), 7.29 (ddd, J = 23.8, 18.3, 11.0 Hz, 17H), 7.15–7.08 (m, 2H). ^{13}C NMR (100 MHz, $CDCl_3$): δ 182.3, 143.0, 141.5, 140.8, 140.6, 140.4, 140.2, 137.3, 137.0, 136.4, 135.6, 134.0, 133.7, 131.0, 130.9, 130.4, 128.6, 127.9, 127.3, 127.2, 127.0, 126.5, 126.0, 125.9, 123.5, 123.3, 120.4, 120.1, 119.9, 109.9, 109.6, 25.6. FTIR (KBr): 3048, 1672, 1595, 1509, 1478, 1448 cm^{-1}; HRMS (APPI-TOF, positive mode) m/z calcd for $C_{96}H_{58}N_4O_2$ 1299.4593; found 1299.4592 $[M]^+$.

7,12-Bis(bis(pyren-1-yl)methylene)-7,12-dihydropentacene-5,14-dione (5c). Compound **5c** was obtained according to the general procedure (0.41 g, 0.36 mmol) in 59% as an orange solid. Mp > 325 °C (decomp.). ^{1}H NMR (400 MHz, DMSO-d_6): δ 9.64–9.35 (m, 3H), 9.00 (d, J = 9.4 Hz, 1H), 8.95–8.76 (m, 4H), 8.70 (d, J = 8.0 Hz, 3H), 8.57 (d, J = 5.1 Hz, 4H), 8.50–8.30 (m, 8H), 8.32–7.94 (m, 18H), 7.68 (d, J = 7.6 Hz, 1H), 7.53–7.39 (m, 2H), 7.36 (s, 1H), 7.22 (d, J = 5.9 Hz, 1H), 6.54–6.43 (m, 1H), 6.38–6.27 (m, 1H). FTIR (KBr): 3037, 1671, 1583, 1485, 1454, 1432 cm^{-1}. HRMS (APPI-TOF, positive mode) m/z calcd for $C_{88}H_{47}O_2$ 1135.3576; found 1135.3553 $[M + H]^{+\bullet}$.

7,12-Bis(bis(benzo[*b*]thiophen-3-yl)methylene)-7,12-dihydropentacene-5,14-dione (5d). Compound **5d** was obtained according to the general procedure (0.30 g, 0.35 mmol) in 57%

yield as a green-yellow solid. Mp > 335 °C (decomp.). ^{1}H NMR (400 MHz, $CDCl_3$): δ 8.23 (s, 2H), 8.07 (dd, J = 5.7, 3.3 Hz, 2H), 7.95 (d, J = 8.1 Hz, 2H), 7.84 (d, J = 8.3 Hz, 3H), 7.82–7.77 (m, 5H), 7.65–7.60 (m, 4H), 7.30 (t, J = 7.5 Hz, 2H), 7.23 (t, J = 2.8 Hz, 2H), 7.20 (d, J = 8.3 Hz, 2H), 7.13 (t, J = 7.6 Hz, 2H), 6.96 (m, 2H), 6.66 (dd, J = 5.8, 3.3 Hz, 2H). ^{13}C NMR (100 MHz, $CDCl_3$): δ 182.1, 142.5, 140.1, 140.0, 138.0, 137.8, 137.5, 136.8, 136.3, 136.0, 133.6, 133.4, 130.6, 129.5, 127.1, 127.0, 126.7, 126.3, 126.1, 125.9, 124.4, 124.4, 123.0, 123.0, 122.9, 122.6. FTIR (KBr): 3062, 1674, 1587, 1511, 1453, 1425 cm^{-1}. HRMS (APPI-TOF, positive mode) m/z calcd for $C_{56}H_{31}O_2S_4$ 863.1207; found 863.1194 $[M + H]^{+\bullet}$.

Conflicts of interest

There are no conflicts to declare.

Acknowledgements

The authors thank the financial support by the Deanship of Scientific Research at the Hashemite University (grant number 24-2021). F. S. and Y. Z. acknowledge the funding support from the Natural Sciences and Engineering Research Council of Canada (NSERC) and Canada Foundation for Innovation (CFI). Dr Jian-Bin Lin at C-CART, Memorial University of Newfoundland is acknowledged for collecting the single-crystal XRD data and solving the crystal structures. Prof. Karl Jobst at Memorial University is acknowledged for assistance in the HRMS analysis. The Digital Research Alliance of Canada (the Alliance) is acknowledged for assistance in our computational modeling studies.

Notes and references

1 J. Yang, D. Yan and T. S. Jones, *Chem. Rev.*, 2015, **115**, 5570–5603.
2 X. Wan, C. Li, M. Zhang and Y. Chen, *Chem. Soc. Rev.*, 2020, **49**, 2828–2842.
3 J. Zhao, C. Yao, M. U. Ali, J. Miao and H. Meng, *Mater. Chem. Front.*, 2020, **4**, 3487–3504.
4 J. Zhao, J. Ren, G. Zhang, Z. Zhao, S. Liu, W. Zhang and L. Chen, *Chem.–Eur. J.*, 2021, **27**, 10781–10797.
5 L. Duan, J. Qiao, Y. Sun and Y. Qiu, *Adv. Mater.*, 2011, **23**, 1137–1144.
6 N. R. Armstrong, W. Wang, D. M. Alloway, D. Placencia, E. Ratcliff and M. Brumbach, *Macromol. Rapid Commun.*, 2009, **30**, 717–731.
7 P. Ledwon, *Org. Electron.*, 2019, **75**, 105422.
8 Y. Liu, Y. Wu, Y. Geng, E. Zhou and Y. Zhong, *Adv. Funct. Mater.*, 2022, **32**, 2206707.
9 Y. Zheng and J. Xue, *Polym. Rev.*, 2010, **50**, 420–453.
10 S. Holliday, Y. Li and C. K. Luscombe, *Prog. Polym. Sci.*, 2017, **70**, 34–51.
11 J. Zhang, J. Jin, H. Xu, Q. Zhang and W. Huang, *J. Mater. Chem. C*, 2018, **6**, 3485–3498.
12 I. Osaka, T. Abe, M. Shimawaki, T. Koganezawa and K. Takimiya, *ACS Macro Lett.*, 2012, **1**, 437–440.
13 Y. Wang and T. Michinobu, *J. Mater. Chem. C*, 2016, **4**, 6200–6214.
14 C. Pigot, G. Noirbent, D. Brunel and F. Dumur, *Eur. Polym. J.*, 2020, **133**, 109797.
15 A. Mau, T. H. Le, C. Dietlin, T.-T. Bui, B. Graff, F. Dumur, F. Goubard and J. Lalevee, *Polym. Chem.*, 2020, **11**, 7221–7234.
16 Y. Chen, D. Zhang, Y. Zhang, X. Zeng, T. Huang, Z. Liu, G. Li and L. Duan, *Adv. Mater.*, 2021, **33**, 2103293.
17 H. Zhou, Q. Huang, X. Liu, D. Xu, W. Zhang, S. Fu, X. Feng and Z. Zhang, *Dyes Pigm.*, 2021, **184**, 108868.
18 M. Hayashi, K. Otsubo, T. Kato, K. Sugimoto, A. Fujiwara and H. Kitagawa, *Chem. Commun.*, 2015, **51**, 15796–15799.
19 J. Roncali, P. Leriche and P. Blanchard, *Adv. Mater.*, 2014, **26**, 3821–3838.
20 X. Cheng, M. Li, Z. Guo, J. Yu, G. Lu, L. Bu, L. Ye, H. Ade, Y. Chen and Y. Geng, *J. Mater. Chem. A*, 2019, **7**, 23008–23018.
21 H. Chen, X. Xia, J. Yuan, Q. Wei, W. Liu, Z. Li, C. Zhu, X. Wang, H. Guan, X. Lu, *et al.*, *ACS Appl. Mater. Interfaces*, 2021, **13**, 36053–36061.
22 C. Duan, R. E. Willems, J. J. van Franeker, B. J. Bruijnaers, M. M. Wienk and R. A. Janssen, *J. Mater. Chem. A*, 2016, **4**, 1855–1866.
23 D. Seo, Y. Yoon, H. M. Yeo, K.-K. Lee, B. Kim and K. Kwak, *Bull. Korean Chem. Soc.*, 2015, **36**, 513–519.
24 B. Tu, Y. Wang, W. Chen, B. Liu, X. Feng, Y. Zhu, K. Yang, Z. Zhang, Y. Shi, X. Guo, *et al.*, *ACS Appl. Mater. Interfaces*, 2019, **11**, 48556–48563.
25 D. Li, H. Lu, Y.-N. Chen, X. Ma, H. Zhang, H. Wang, X. Yu, X. Xu, Z. Zhang, X. Xu, *et al.*, *Chem. Mater.*, 2022, **34**, 8840–8848.
26 H. Moon, R. Zeis, E.-J. Borkent, C. Besnard, A. J. Lovinger, T. Siegrist, C. Kloc and Z. Bao, *J. Am. Chem. Soc.*, 2004, **126**, 15322–15323.
27 Z.-F. Yao, J.-Y. Wang and J. Pei, *Cryst. Growth Des.*, 2018, **18**, 7–15.
28 K. Nakahara, C. Mitsui, T. Okamoto, M. Yamagishi, K. Miwa, H. Sato, A. Yamano, T. Uemura and J. Takeya, *Chem. Lett.*, 2013, **42**, 654–656.
29 M. Gsänger, J. H. Oh, M. Könemann, H. W. Höffken, A.-M. Krause, Z. Bao and F. Würthner, *Angew. Chem., Int. Ed.*, 2010, **49**, 740–743.
30 Z. Chen, M. G. Debije, T. Debaerdemaeker, P. Osswald and F. Würthner, *ChemPhysChem*, 2004, **5**, 137–140.
31 C.-H. Liu, M. R. Niazi and D. F. Perepichka, *Angew. Chem., Int. Ed.*, 2019, **58**, 17312–17321.
32 R. Rathore and J. K. Kochi, *Adv. Phys. Org. Chem.*, 2000, **35**, 193–318.
33 E. J. Son, J. H. Kim, K. Kim and C. B. Park, *J. Mater. Chem. A*, 2016, **4**, 11179–11202.
34 Y. Misaki, S. Noda, M. Kato, T. Yamauchi, T. Oshima, A. Yoshimura, T. Shirahata and M. Yao, *ChemSusChem*, 2020, **13**, 2312–2320.
35 Y. Cui, J. Liu, Z. Li, M. Ji, M. Zhao, M. Shen, X. Han, T. Jia, C. Li and Y. Wang, *Adv. Funct. Mater.*, 2021, **31**, 2106247.

36 M. Yamaji, T. Itoh and S. Tobit, *Photochem. Photobiol. Sci.*, 2002, **1**, 869–876.
37 E. A. Younes and Y. Zhao, *Org. Chem. Front.*, 2017, **4**, 804–810.
38 D. Käfer, M. El Helou, C. Gemel and G. Witte, *Cryst. Growth Des.*, 2008, **8**, 3053–3057.
39 Y. Ishigaki, T. Harimoto, K. Sugawara and T. Suzuki, *J. Am. Chem. Soc.*, 2021, **143**, 3306–3311.
40 M. F. Abdollahi and Y. Zhao, *J. Org. Chem.*, 2021, **86**, 14855–14865.
41 A. Heckmann and C. Lambert, *J. Am. Chem. Soc.*, 2007, **129**, 5515–5527.
42 C. Lambert, J. Schelter, T. Fiebig, D. Mank and A. Trifonov, *J. Am. Chem. Soc.*, 2005, **127**, 10600–10610.
43 A. Farokhi, H. Shahroosvand, F. Zisti, M. Pilkington and M. K. Nazeeruddin, *J. Mater. Chem. A*, 2023, **11**, 25136–25215.
44 Y. Li, S. S. Rajasree, G. Y. Lee, J. Yu, J.-H. Tang, R. Ni, G. Li, K. N. Houk, P. Deria and P. J. Stang, *J. Am. Chem. Soc.*, 2021, **143**, 2908–2919.
45 A. Farokhi, H. Shahroosvand, G. D. Monache, M. Pilkington and M. K. Nazeeruddin, *Chem. Soc. Rev.*, 2022, **51**, 5974–6064.
46 A. Cravino, S. Roquet, O. Alévêque, P. Leriche, P. Frere and J. Roncali, *Chem. Mater.*, 2006, **18**, 2584–2590.
47 S. Matsuda, C. Itagaki, K. Tatsuguchi, M. Ito, H. Sasaki and M. Umeda, *Sci. Rep.*, 2022, **12**, 7294.
48 H. F. Higginbotham, P. Pander, R. Rybakiewicz, M. K. Etherington, S. Maniam, M. Zagorska, A. Pron, A. P. Monkman and P. Data, *J. Mater. Chem. C*, 2018, **6**, 8219–8225.
49 Z. Yin, X. Chang, J. Zang, S. Lin, Z. Zhou, T. Liu, L. Ding, H. Peng and Y. Fang, *J. Mater. Chem. C*, 2022, **10**, 10429–10438.
50 S. Sau and S. K. Samanta, *Chem. Commun.*, 2023, **59**, 635–638.
51 E. A. Younes and Y. Zhao, *RSC Adv.*, 2015, **5**, 88821–88825.
52 A. Babaei, P. A. Connor, A. J. McQuillan and S. Umapathy, *J. Chem. Educ.*, 1997, **74**, 1200.
53 P. Blanchard, C. Malacrida, C. Cabanetos, J. Roncali and S. Ludwigs, *Polym. Int.*, 2019, **68**, 589–606.
54 O. Dolomanov, L. Bourhis, R. Gildea and J. Howard, *J. Appl. Crystallogr.*, 2009, **42**, 339–341.
55 G. M. Sheldrick, *Acta Crystallogr., Sect. A: Found. Adv.*, 2015, **71**, 3–8.
56 G. M. Sheldrick, *Acta Crystallogr., Sect. C: Struct. Chem.*, 2015, **71**, 3–8.
57 M. J. Frisch, G. W. Trucks, H. B. Schlegel, G. E. Scuseria, M. A. Robb, J. R. Cheeseman, G. Scalmani, V. Barone, G. A. Petersson, H. Nakatsuji, X. Li, M. Caricato, A. V. Marenich, J. Bloino, B. G. Janesko, R. Gomperts, B. Mennucci, H. P. Hratchian, J. V. Ortiz, A. F. Izmaylov, J. L. Sonnenberg, D. Williams-Young, F. Ding, F. Lipparini, F. Egidi, J. Goings, B. Peng, A. Petrone, T. Henderson, D. Ranasinghe, V. G. Zakrzewski, J. Gao, N. Rega, G. Zheng, W. Liang, M. Hada, M. Ehara, K. Toyota, R. Fukuda, J. Hasegawa, M. Ishida, T. Nakajima, Y. Honda, O. Kitao, H. Nakai, T. Vreven, K. Throssell, J. A. Montgomery Jr, J. E. Peralta, F. Ogliaro, M. J. Bearpark, J. J. Heyd, E. N. Brothers, K. N. Kudin, V. N. Staroverov, T. A. Keith, R. Kobayashi, J. Normand, K. Raghavachari, A. P. Rendell, J. C. Burant, S. S. Iyengar, J. Tomasi, M. Cossi, J. M. Millam, M. Klene, C. Adamo, R. Cammi, J. W. Ochterski, R. L. Martin, K. Morokuma, O. Farkas, J. B. Foresman and D. J. Fox, *Gaussian 16 Revision B.01*, Gaussian Inc., Wallingford CT, 2016.
58 E. F. Pettersen, T. D. Goddard, C. C. Huang, E. C. Meng, G. S. Couch, T. I. Croll, J. H. Morris and T. E. Ferrin, *Protein Sci.*, 2021, **30**, 70–82.